Available online at website: https://journal.bcrec.id/index.php/bcrec

Bulletin of Chemical Reaction Engineering & Catalysis, 21 (2) 2026, 370-384

Original Research Article

Enhanced Photocatalytic Performance and Kinetic Improvement of Reusable W-based POM Composite for Produced Water Treatment

Tutuk Djoko Kusworo*, Andri Cahyo Kumoro, Adalia Veda, Rafi Mafazan, Meitri Bella Puspa, Dita Aulia Azizah

Department of Chemical Engineering, Faculty of Engineering, Diponegoro University, Jl. Prof. Soedarto, Semarang, 50275, Indonesia.

Received: 3rd January 2026; Revised: 11th February 2026; Accepted: 11th February 2026
Available online: 15th February 2026; Published regularly: August 2026

Abstract

Produced water treatment remains a major challenge due to its complex contaminant composition and the limited efficiency and reusability of conventional photocatalysts. Polyoxometalate (POM)-based materials offer high redox activity and structural tunability. This study presents a novel tungsten-based polyoxometalate (W-based POM) composite with enhanced photocatalytic performance and kinetic superiority for produced water treatment. The objective of this work was to synthesize a reusable W-based POM composite and systematically evaluate its photocatalytic activity, adsorption behavior, kinetics, and stability. The composite was synthesized via a solvothermal method using $Na_2WO_4 \cdot 2H_2O$ and DMF. Photocatalytic experiments were performed by varying catalyst dosage (0.1–0.5 g), irradiation time (30-180 min), and reusability cycles. The W-based POM composite exhibited a rhombic polyhedral morphology with a well-organized three-dimensional POM framework, reduced crystallite size (14.8 nm), and compressive lattice strain, contributing to improved charge mobility. Optical analysis revealed a red-shift in the absorption edge, reducing the band gap from 2.80 eV to 2.25 eV and enhancing visible-light utilization. Photocatalytic experiments demonstrated high treatment efficiency, achieving 90% NH_3–N and 84% total dissolved solids (TDS) removal under UV irradiation within 180 minutes at an optimal dosage of 0.3 g. Adsorption behavior followed the Dubinin–Radushkevich and Temkin isotherm models, indicating an ion-exchange-dominated mechanism, while kinetic analysis revealed a multi-step process governed by intraparticle diffusion. The composite maintained stable performance over three consecutive cycles without significant activity loss. Overall, the results highlight the strong potential of W-based POM composites as efficient, reusable, and scalable photocatalysts for advanced produced water treatment.

Keywords: Polyoxometalate (POM); photocatalysis; produced water treatment; adsorption isotherms; band-gap engineering

How to Cite: Kusworo, T. D., Kumoro, A. C., Veda, A., Mafazan, R., Puspa, M. B., Azizah, D. A., Utomo, D. P. (2026). Enhanced Photocatalytic Performance and Kinetic Improvement of Reusable W-based POM Composite for Produced Water Treatment. *Bulletin of Chemical Reaction Engineering & Catalysis*, 21 (2), 370-384. (DOI: 10.9767/bcrec.20616)

Permalink/DOI: https://doi.org/10.9767/bcrec.20616

1. Introduction

According to the World Resources Institute's 2023 report, approximately 4 billion people, equivalent to half of the global population, experience water scarcity every month, a figure projected to reach 60% by 2025 [1]. The surge in water demand has been evident since the 1960s, primarily driven by rapid population growth and expansion across agricultural, livestock, manufacturing, and energy sectors. These industries not only require substantial water input but also discharge significant volumes of wastewater, further depleting natural freshwater reserves [2]. The petrochemical industry, in particular, is recognized as a major contributor, consuming 2–3 gallons of water for every gallon of crude oil processed [3,4]. The resulting produced water (PRW) often contains a complex mix of pollutants, including oil, grease, phenols, heavy metals, ammonia, aromatic hydrocarbons, and hydrogen sulfide, frequently in elevated

* Corresponding Author.
Email: tdkusworo@che.undip.ac.id (T.-D. Kusworo)

concentrations. Such contaminants disrupt ecological balance and pose serious health risks to nearby communities. Jala *et al.* reported that phenols interfere with human metabolic pathways [5]; aromatic hydrocarbons can impair vital systems such as the immune, nervous, and hepatic systems, potentially leading to cancer [6]; heavy metals may cause acute toxicity [7]; and ammonia, a prevalent PRW pollutant, is associated with liver damage, intestinal cancer, and methemoglobinemia [8]. As a result, global environmental organizations have emphasized the urgent need to manage PRW effectively, as its uncontrolled discharge not only worsens global water scarcity but also endangers ecosystems and public health. Proper treatment of PRW can simultaneously enhance industrial productivity and contribute to sustainable global water availability.

Various treatment strategies have been explored to manage produced water (PRW), including coagulation and electrocoagulation [9], [10], ion-exchange [11], activated sludge [12], advanced oxidation processes (AOPs) [13], and membrane filtration . While these approaches have yielded promising results, their high operational and capital costs have limited large-scale implementation, particularly in industrial settings. Among the alternatives, photocatalytic degradation has emerged as one of the most efficient and practical methods due to its ability to initiate photo-redox reactions by converting photonic energy into chemical energy. Titanium dioxide (TiO_2) is widely known for its role in heterogeneous photocatalysis owing to its ability to absorb ultraviolet (UV) light, alongside its advantages such as chemical stability, non-toxicity, low cost, and high reactivity. However, its large band gap (3.2 eV) restricts its activation to UV light, which accounts for less than 4% of the solar spectrum, thereby limiting its photocatalytic efficiency. This limitation leads to rapid recombination of photogenerated electron–hole pairs and poor photo-induced reaction performance. Consequently, UV lamp supplementation is often required, further increasing operational costs. Despite the effectiveness of existing photocatalytic systems, a major unresolved issue in produced water treatment is achieving high contaminant removal efficiency while maintaining favorable reaction kinetics and catalyst reusability under realistic operating conditions. Many reported photocatalysts exhibit promising degradation efficiencies. However, limited attention has been given to kinetic behavior and long-term stability in complex PRW matrices, which hampers their practical and scalable application.

To overcome this challenge, research continues to focus on developing photocatalysts that can efficiently utilize the abundant visible light in natural sunlight. Tungsten trioxide (WO_3) has attracted attention due to its favorable optical, chemical, and electrochemical properties, offering greater stability than TiO_2. With a narrower band gap (2.8 eV), WO_3 can absorb a broader portion of the visible spectrum. Additionally, its resistance to photocorrosion and ability to store photogenerated energy ("round-the-clock photocatalysis") enhance its application potential [14,15]. However, bulk WO_3 is often limited by its low surface area, attributed to its dense crystalline structure, and by high electron–hole recombination rates, which stem from its intrinsic tensile strain properties [16,17].

Polyoxometalates (POMs) are metal oxyanion clusters primarily composed of transition metals such as Mo, W, V, Nb, and Tb in their highest oxidation states [18]. The incorporation of substituted metals or other cations into the POM structure can effectively regulate their physical and chemical properties. POMs are also well-known for their ability to undergo multi-electron reversible redox reactions without significant structural alteration [19]. Considering the advantageous properties of bulk WO_3, the development of W-based POM composites presents a promising strategy to overcome the limitations of the parent material. In this study, a W-based polyoxometalate composite was synthesized via a solvothermal method using sodium tungstate dihydrate ($Na_2WO_4 \cdot 2H_2O$) to address the combined challenges of photocatalytic efficiency, kinetic performance, and reusability in produced water treatment. Comprehensive characterization, including morphological, structural, and optical analysis, was conducted to evaluate the enhanced features of the synthesized composite. The study also investigated the optimal dosage of the composite, irradiation time, and reuse cycles on the photocatalytic removal of ammonia nitrogen (NH_3-N) and total dissolved solids (TDS) selected as the main target pollutants. Furthermore, adsorption isotherms and kinetic models were explored in-depth to understand the interaction mechanisms and rate-controlling steps of the adsorption process, respectively. Despite extensive studies on photocatalytic materials for wastewater treatment, kinetic analyses are still largely limited to simplified pseudo-first-order or pseudo-second-order models, which inadequately describe the complex mass transfer and diffusion phenomena in real produced water systems. In heterogeneous photocatalysis, adsorption plays a critical role in controlling pollutant transport to active sites and governing overall degradation efficiency**.** Adsorption–diffusion-based kinetic models, such as intraparticle diffusion, Elovich, and Bangham's models, remain underexplored despite their potential to elucidate multi-step removal mechanisms Accordingly, this study

integrates adsorption isotherm analysis with advanced kinetic modeling to provide a more realistic and mechanistic interpretation of photocatalytic produced water treatment. Reusability tests confirmed the stability and durability of the composite, highlighting its potential for future application, either as a primary or hybrid material, in industrial-scale PRW treatment systems.

2. Materials and Methods

2.1 Materials

The raw produced water used as the sample in this study was obtained from Refinery Unit VI, PT. Pertamina Balongan, West Java, Indonesia, with its characteristics summarized in Table 1. The primary reagents used for material synthesis included sodium tungstate dihydrate ($Na_2WO_4 \cdot 2H_2O$, ≥99%), N,N-dimethylformamide (DMF, ≥99.8%), and terephthalic acid (H_2BDC, 98%), all of which were procured from Sigma-Aldrich, Singapore. In addition, bulk tungsten trioxide (WO_3, 99%) and anhydrous ethanol (C_2H_5OH, ≥97%) were obtained from Lab Chemicals, USA. Distilled water used throughout the experimental procedures was supplied by the university's reverse osmosis (RO) filtration system. All chemicals were of analytical grade and used as received without any further purification.

2.2. Synthesis of W-based POM Composite

W-based polyoxometalate (POM) composites were synthesized based on the method previously reported by Chen *et al.* [20]. $Na_2WO_4 \cdot 2H_2O$, H_2BDC, and DMF were mixed in a molar ratio of 1:1:100 in a 100 mL beaker. The resulting solution was stirred at moderate speed for 30 minutes and subsequently transferred into a 100 mL Teflon-lined stainless-steel autoclave. The autoclave was then sealed and heated at 150 °C for 10 h under solvothermal conditions. After cooling to room temperature, the resulting product was washed alternately with distilled water and anhydrous ethanol several times to remove residual impurities. The suspension was then left to stand overnight in ethanol. The final product was dried at 100 °C for 10 h, ground into fine powder, and collected as the W-based POM composite.

2.3. Characterization of the Composites

Morphological characteristics and elemental composition, including spatial distribution, of the composites were analyzed using a scanning electron microscope equipped with energy-dispersive X-ray spectroscopy (SEM-EDX, JEOL Series LA, Japan). The crystalline structure and phase purity of the composites were further evaluated by X-ray diffraction (XRD, Shimadzu, Japan) over a 2θ range of 10–90°, using Cu-Kα radiation and a scanning rate of 4°/min. The optical properties of the composite were assessed using a UV–Vis spectrophotometer (Shimadzu, Japan) within a wavelength range of 250–800 nm. In addition, a 10 W artificial UV-C lamp (Philips) was employed as the photon source during the photocatalytic degradation experiments.

2.4. A Simultaneous Adsorption-Photocatalytic Activity Measurement

As a preliminary investigation, determining the optimal dosage of the composite was essential. For this purpose, the adsorption–photocatalytic activity was evaluated at varying dosages of 0.1, 0.3, and 0.5 g. Each experiment was conducted under identical conditions, using 100 mL of produced water (PRW) and placing the sample at a fixed distance (10 cm) beneath a UV lamp. The overall reaction time was maintained at 180 minutes, during which aliquots were collected at predetermined time intervals. The collected samples were centrifuged, and the supernatants were analyzed to determine the concentrations of NH_3-N and total dissolved solids (TDS). NH_3-N content was measured using a UV–Vis spectrophotometer in conjunction with the HI3824-025 reagent kit, while TDS values were obtained using a standard TDS meter. The pollutant removal efficiency (R, %) and adsorption capacity (Q_e, mg/g) were calculated using the following Equations (1) and (2) [21]:

$$R = \frac{C_0 - C_e}{C_0} \times 100\% \quad (1)$$

$$Q_e = \frac{C_0 - C_e}{m} \times V \quad (2)$$

Where C_0, C_e, m, and V are the initial and the equilibrium pollutant concentration at time t (mg/L), the mass of the composite, and the volume of the PRW sample (L), respectively.

2.5. Adsorption Isotherms

The adsorption isotherm of the W-based POM composite was comprehensively analyzed using several models, including Langmuir, Freundlich, Temkin, and Dubinin–Radushkevich (D–R), with their respective mathematical expressions presented in Equations (3)–(6) [22,23].

$$\frac{1}{Q_e} = \frac{1}{K_L Q_m C_e} + \frac{1}{Q_m}; R_L = \frac{1}{1 + K_L C_0} \quad (3)$$

$$log\, Q_e = log\, K_F + \frac{1}{n} log\, C_e \quad (4)$$

$$Q_e = \frac{RT}{b_T} ln\, K_T + \frac{RT}{b_T} ln\, C_e \quad (5)$$

$$ln\, Q_e = ln\, Q\, m - \beta \varepsilon^2 \quad (6)$$

where Q_m, K_L, R_L represent the maximum adsorption capacity (mg/g), the Langmuir isotherm constant (L.mg^{-1}), and the Langmuir separation factor, respectively. Meanwhile, K_F, n,

K_T, b_T, β, and ε are the Freundlich isotherm constant (L.mg^{-1}), adsorption intensity, Temkin isotherm constant (L.mg^{-1}), Temkin constant related to the heat of adsorption (J.mol^{-1}), *DR* constant related to adsorption energy (mol^2.kJ^2), and Polanyi potential (kJ.mol^{-1}), respectively. R and T denote the universal gas constant (8.314 J.mol^{-1}.K^{-1}) and the adsorption operating temperature (303.15 K), respectively.

2.6. Adsorption Kinetics

The exploration of the rate-controlling steps in the adsorption process was conducted using several kinetic models, including pseudo-first-order (PFO), pseudo-second-order (PSO), intraparticle diffusion (ID), Elovich, and Bangham's models, with their corresponding mathematical expressions presented in Equations (7)–(11), respectively [24-26].

$$ln(Q_e - Q_t) = ln\, Q_e - K_1 t \quad (7)$$

$$\frac{t}{Qt} = \frac{1}{K_2 Q_e^2} - \frac{t}{Q_e} \quad (8)$$

$$Q_t = K_{id} t^{0.5} + C_i \quad (9)$$

$$Q_t = \frac{1}{\beta} ln(\alpha\beta) + \frac{1}{\beta} ln\, t \quad (10)$$

$$log\left[log\left(\frac{C_0}{C_0 - Q_t \cdot m}\right)\right] = log(k) + n \cdot log(t) \quad (11)$$

Where Q_t and Q_e are the pollutant adsorption capacity at certain time (mg.g^{-1}) and the equilibrium adsorption capacity (mg.g^{-1}), while K_1, K_2, and K_{id}, represent the kinetics constants of PFO (min^{-1}), PSO (g.mg^{-1}.min^{-1}), and *ID* (mg.(g.min)$^{0.5}$). The α and β in the Elovich equation represent the initial desorption rate (mg.g^{-1}.min^{-1}) and desorption constant or activation energy coefficient (g.mg^{-1}), while k and n are Bangham's constant.

2.7. Reusability and Stability

The reusability and structural stability of the W-based POM composite were evaluated to determine its long-term performance and economic feasibility for produced water treatment. The photocatalyst was subjected to three consecutive photocatalytic degradation cycles under identical operating conditions, including catalyst dosage, irradiation intensity, reaction time, and initial produced water composition. At the end of each cycle, the W-based POM composite was recovered by filtration, thoroughly rinsed with deionized water to remove residual contaminants, and regenerated by drying at 100 °C for 10 h. A fresh produced water (PRW) sample was used as the feed solution for each subsequent cycle to eliminate interference from residual pollutants. The photocatalytic performance during each cycle was evaluated based on the removal efficiencies.

3. Results and Discussion

3.1. Characterization of W-based POM nanocomposite

3.1.1. Morphology and Elemental Composition Evaluation

Morphological analysis is essential to evaluate the actual appearance of the fabricated material. Surface observation was carried out using a Scanning Electron Microscope (SEM) at a magnification of 1000×. As shown in Figure 1(A), the fabricated W-based POM exhibits a

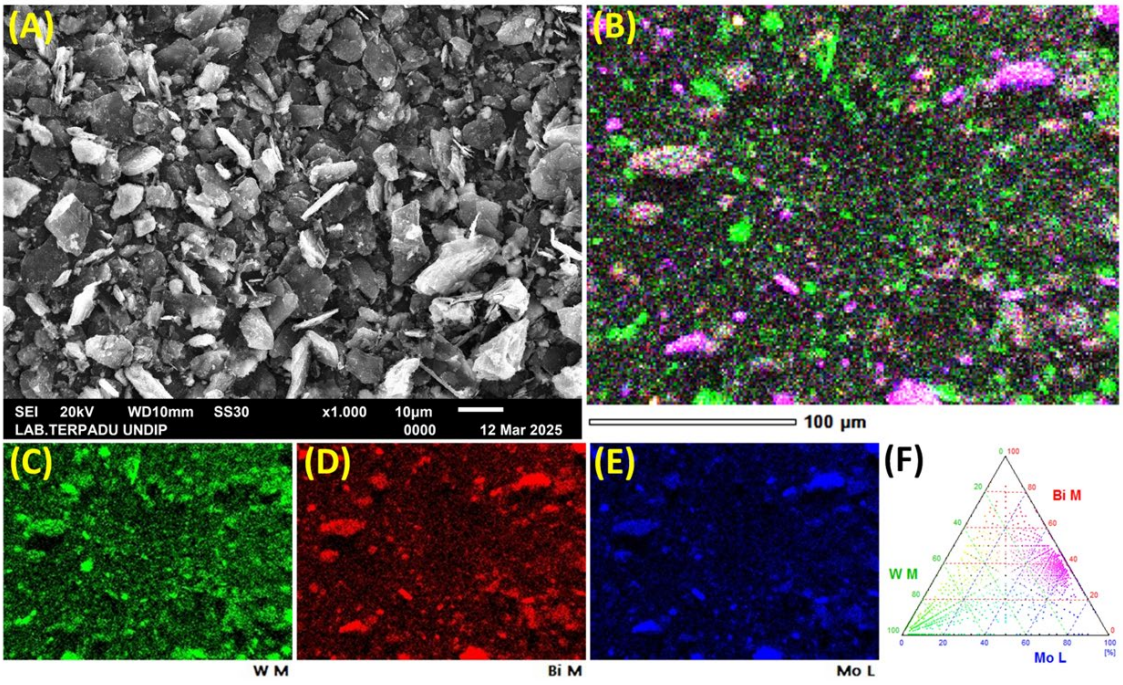

Figure 1. (A) SEM image, (B) SEM-EDX mapping, followed by its materials constituent (C) Tungsten (W), (D) Bi (Bismuth), (E) Mo (Molybdenum), and (F) their ternary diagram in W-based POM composite.

homogeneous morphological structure with a three-dimensional framework, predominantly characterized by rhombic polyhedra with tapered ends and a broad midsection, in agreement with previous reports [20,27]. The relatively large particle size (l: 9.72 ± 0.70 µm; w: 7.19 ± 1.31 µm) reflects the material's high crystallinity and mechanical robustness, making it suitable for extended applications. The observed morphology is likely attributed to the solvothermal synthesis route, which enables a controlled environment for tuning the structure, crystallinity, particle size, acidity, and the spatial positioning of POM units [28]. Figure 1(B) displays the elemental mapping of the nanocomposite, clearly indicating the uniform distribution of the dominant elements, tungsten (W), bismuth (Bi), and molybdenum (Mo), as shown in Figure 1(C–E), respectively. A ternary diagram [Figure 1(F)] further illustrates the interactions among these elements: Bi and Mo appear to co-localize, producing a purple color in the mapping overlay, while W is spatially separated, likely forming tungstate salts and thus confirming the formation of the W-based POM 3D framework. Although direct evidence remains limited, the EDX characterization provides a convincing depiction of the successful fabrication of the material.

3.1.2. Structure evaluation

The phase, crystal structure, and crystallinity of the materials were analyzed using X-ray diffraction (XRD). Nano-WO_3 was employed as a reference material due to its status as the predominant oxide form of tungsten under ambient conditions. As shown in Figure 2(A), the WO_3 photocatalyst exhibits distinct diffraction peaks at 2θ = 23.18°, 23.68°, 24.42°, 26.68°, 28.78°, 33.34°, 35.48°, 41.98°, 47.28°, 49.98°, 55.98°, 62.28°, and 71.98°, corresponding to the (100), (002), (110), (101), (112), (111), (201), (300), (002), (220), (221), (401), and (222) crystal planes, respectively, which are characteristic of the hexagonal phase of WO_3 (PDF#33-1387) . In contrast, the W-based POM composite displayed a distinct diffraction pattern, reflecting its polycrystalline nature (88.58%) and structural deviation from bulk WO_3. Several new diffraction peaks were observed at 2θ = 13.04°, 17.06°, 27.90°, and 32.8°, while other peaks were present with significantly enhanced intensity, indicating the successful formation of tungsten-based POMs. In addition to the influence of precursor composition, the prominent peaks in the 2θ range of 10–35° suggest the presence of a short-range ordered structure with open and layered frameworks [29]. The Williamson–Hall (W–H) plot method was employed to estimate both the crystallite size and the intrinsic lattice strain, considering two major broadening contributions: size broadening (β_{size}) and strain broadening (β_{strain}). Figure 2(B-C) illustrate the W–H linear plots of WO_3 and the W-based POM photocatalyst, respectively. Based on the linear

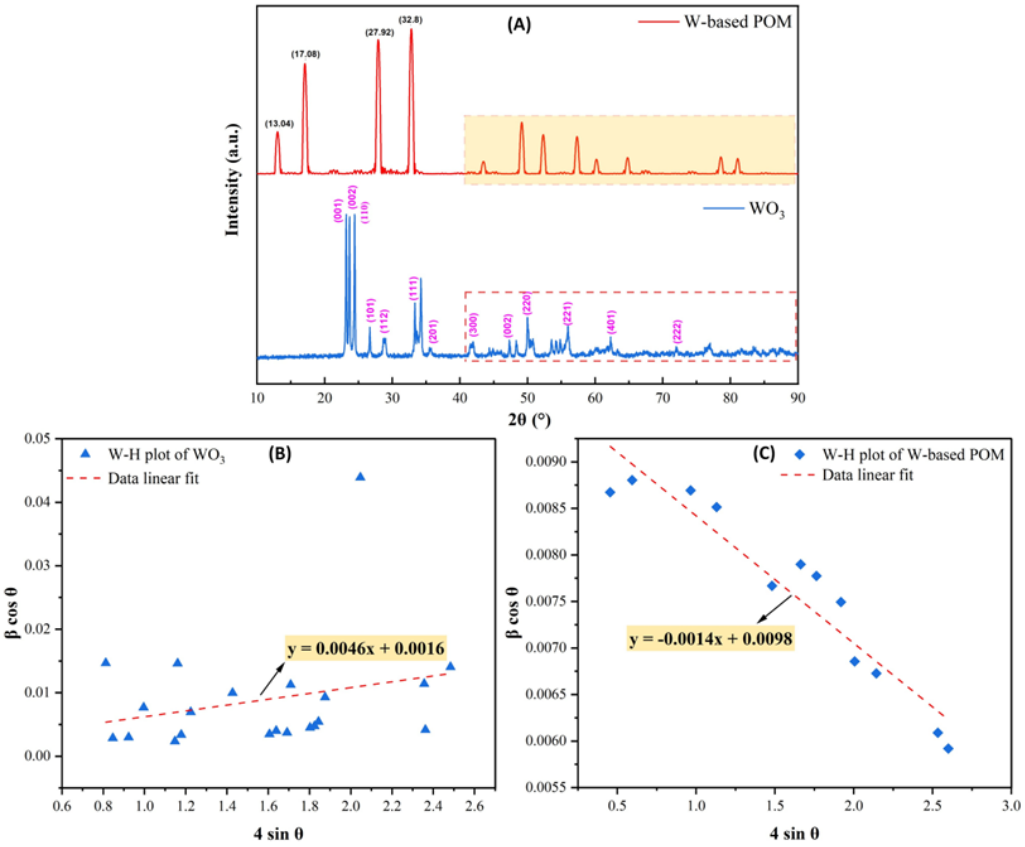

Figure 2. (A) XRD pattern as well as the W-H plot of (B) WO_3 and (C) W-based POM composites.

plot of (4 sin θ) versus (β cos θ), the standard WO_3 sample yielded the linear equation y = 0.0046x + 0.0016, indicating a lattice strain (ε = slope) of 0.0046 and a calculated crystallite size of 90.51 nm from the intercept ($I = k\lambda/D$). Similarly, the W-based POM showed a linear equation of y = -0.0014x + 0.0098, resulting in a lattice strain of ε = -0.0014 and a crystallite size of 14.78 nm. Interestingly, the shift in microstrain characteristics between the two materials is significant. The positive strain value of WO_3 indicates the presence of tensile lattice strain, whereas the negative strain of W-based POM reveals a compressive strain behavior [30]. This alteration in internal strain properties strongly supports the successful transformation of bulk WO_3 into a W-based POM structure. The tensile strain observed in WO_3 is well-documented and is considered inherent to this visible-light-responsive photocatalyst, reflecting its excellent electronic conductivity [14]. In contrast, the compressive strain observed in the synthesized W-based POM is noteworthy, as it not only enhances the intrinsic properties of WO_3 (such as visible-light responsiveness) but also significantly improves charge transport and suppresses charge recombination [31]. The compressive strain behavior is also commonly observed in MIL-53 materials, which exhibit a notable "breathing" behavior - compressing and narrowing pore structures under pressure to enable selective adsorption. Furthermore, the significantly smaller crystallite size of the W-based POM compared to WO_3 suggests enhanced surface area, which increases contact with target pollutants and ultimately improves photocatalytic degradation performance [32].

3.1.3. Optical properties evaluation

Optical analysis plays a crucial role in the development of photocatalysts, providing fundamental insights into their photophysical and photochemical properties. In this study, the absorption edges of the photocatalysts were examined using a UV–Vis spectrophotometer (Shimadzu, Japan) within the spectral range of 250-800 nm, as illustrated in Figure 3(A). A distinct absorption peak was observed for the W-based POM at approximately 300 nm, exhibiting a red shift compared to bulk WO_3, which showed a peak at 250 nm. This red shift indicates a modification in the electronic band structure as a result of structural and compositional adjustments [33]. According to Murmu *et al.* [29], such peak shifts in synthesized photocatalysts are often attributed to the presence of edge-sharing (around 260 nm) and corner-sharing (around 300 nm) oxygen species involved in oxygen-to-tungsten charge transfer processes an indication of the formation

3.2. Performance Evaluation

3.2.1. Catalyst composition effects on produced water degradation efficiency

The influence of catalyst dosage on the degradation efficiency of produced water was systematically investigated by assessing the removal performance of ammonia nitrogen (NH_3–N) and total dissolved solids (TDS) over time using the W-based POM composite at varying dosages (0.1 g, 0.3 g, and 0.5 g). The experimental results, depicted in Figure 4, reveal that both NH_3–N and TDS removal efficiencies are strongly dependent on catalyst dosage and reaction duration. For NH_3–N removal, a progressive increase in degradation efficiency was observed across all catalyst dosages with prolonged contact time, underscoring the temporal enhancement of both adsorption and photocatalytic pathways. Notably, the 0.3 g catalyst dosage exhibited the most effective and stable performance, achieving

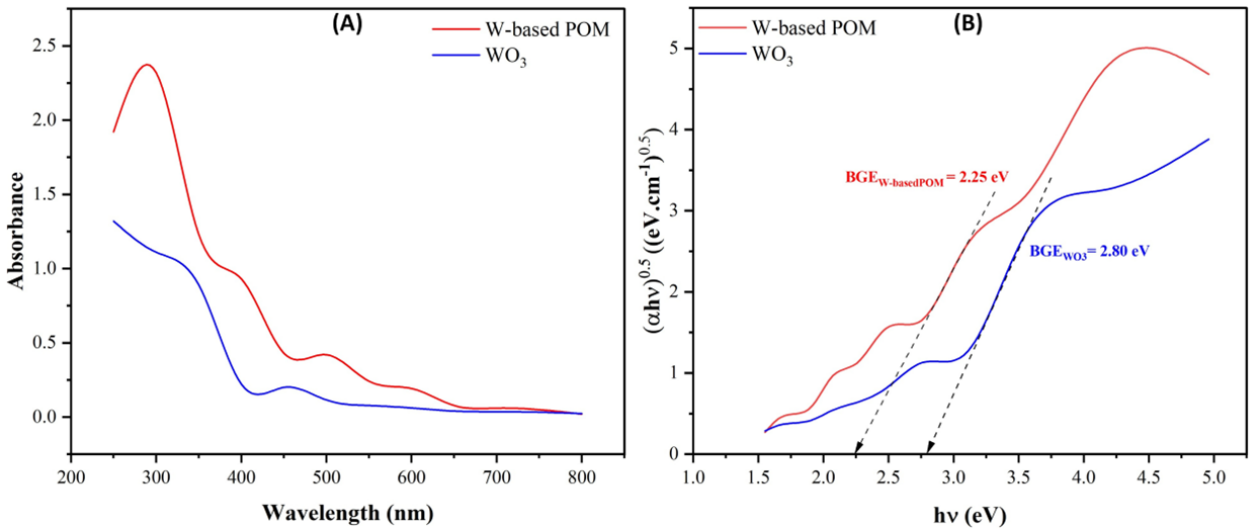

Figure 3. (A) UV-Vis absorbance spectrum and (B) Tauc plot analysis for band gap energy determination of WO_3 and W-based POM composites.

over 90% removal after 180 minutes. In contrast, a further increase in dosage to 0.5 g led to a counterintuitive decline in NH_3–N removal, with the final efficiency reaching only around 80%. The lowest efficiency was recorded at the smallest dosage (0.1 g), which attained approximately 74% removal. This observed phenomenon suggests the existence of an optimal catalyst loading represented here by the 0.3 g dosage, beyond which the degradation performance is hindered rather than enhanced. Several photocatalytic mechanisms can account for this behavior. First, excessive catalyst loading can result in particle agglomeration, reducing the effective surface area accessible for photocatalytic reactions. Second, at higher dosages, the light scattering and shielding effects become pronounced, whereby catalyst particles obstruct light transmission, reducing photon penetration into the suspension [25,34]. As photocatalysis is inherently light-driven, any reduction in light absorption directly limits the generation of reactive oxygen species (ROS), such as hydroxyl and superoxide radicals, which are essential for the degradation of pollutants like NH_3–N. Additionally, oversaturation of active sites can lead to diminished reaction rates due to mass transfer limitations, especially in heterogeneous systems where internal diffusion resistance within porous matrices becomes significant [14].

A comparable trend was observed in the case of TDS removal. The intermediate dosage of 0.3 g again outperformed the others, achieving a final removal efficiency of almost 84%. Interestingly, the 0.5 g dosage performed similarly to or even slightly below the 0.1 g dosage during the earlier stages of the reaction (≤120 minutes), further confirming that excessive catalyst loading can introduce kinetic constraints. Such behavior may be attributed to sedimentation or agglomerate formation that reduces the availability of active catalytic sites in suspension. Furthermore, increased catalyst density can elevate the viscosity and turbidity of the medium, thereby impeding the diffusion of pollutants toward the active surface and reducing the catalyst's overall reactivity. The consistent superior performance of the 0.3 g dosage in both NH_3–N and TDS removal indicates a synergistic balance between available active sites, optimal light absorption, and adequate contaminant–catalyst interactions. This balance is critical in achieving efficient photocatalytic degradation, especially in real wastewater matrices such as produced water, which typically exhibit complex and variable compositions. These findings are consistent with previous studies that have emphasized the importance of catalyst dosage optimization in photocatalytic systems [21,22,35]. For instance, excess catalyst has been shown to impair degradation kinetics due to increased light scattering and recombination of photogenerated charge carriers, which ultimately reduces quantum efficiency. In conclusion, the results underscore the critical role of catalyst composition in optimizing the degradation performance of photocatalytic systems for produced water treatment. The W-based POM composite demonstrates its highest efficacy at an intermediate dosage of 0.3 g, beyond which further increases result in diminishing returns. This highlights the need for careful tuning of catalyst loading in real-world applications, where factors such as reaction kinetics, photon flux, mass transport, and catalyst stability must be concurrently optimized. Such insights pave the way for the rational design of scalable photocatalytic systems for industrial wastewater remediation.

3.2.2. Adsorption isotherm modeling of produced water removal using W-based POM composite

To further elucidate the interaction mechanism between the W-based POM composite

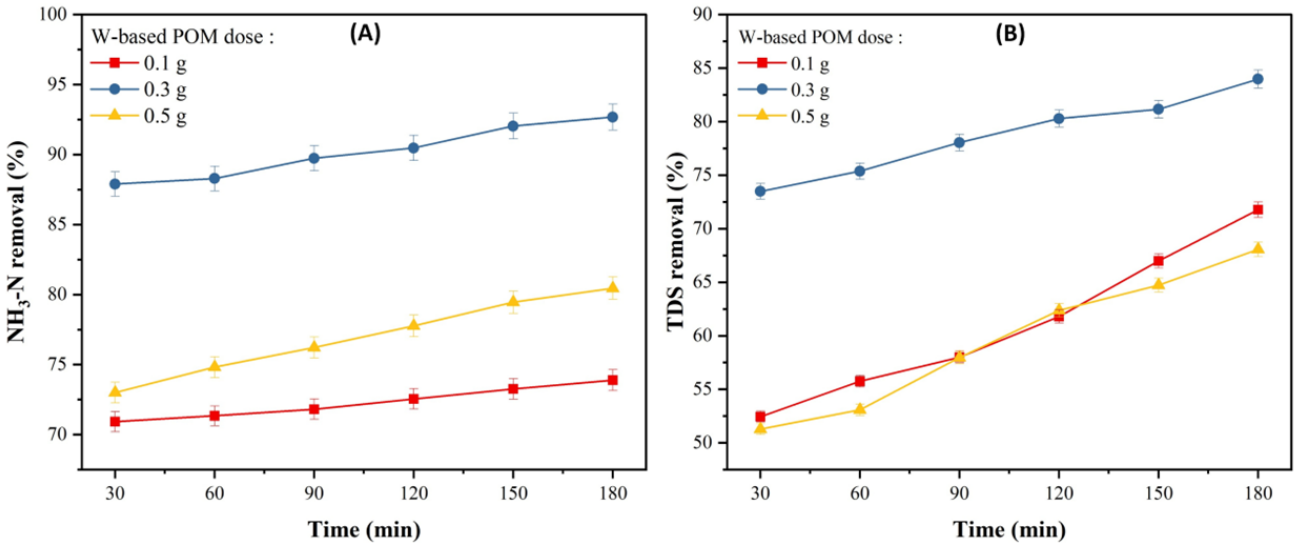

Figure 4. (A) NH_3-N and (B) TDS removal performance of W-based POM composite.

and the organic contaminants present in produced water, adsorption isotherm models were applied to fit the experimental equilibrium data. The modeling was conducted using four classical isotherms: Langmuir, Freundlich, Temkin, and Dubinin–Radushkevich (D–R), which shown by Figure 5 (A-D), respectively, while the corresponding isotherm parameters and correlation coefficients (R^2) are summarized in Table 1. The Langmuir isotherm model, which assumes monolayer adsorption on a homogeneous surface with finite and identical sites, yielded a maximum adsorption capacity (Q_m) of 20.125 mg/g and a Langmuir constant (K_L) of 0.002 L/mg. The relatively high correlation coefficient (R^2 = 0.8775) indicates a good fit, suggesting the presence of uniform adsorption sites on the W-based POM surface. Additionally, the dimensionless separation factor (R_L = 0.479-0.821) falls within the range of $0 < R_L < 1$, confirming the favorable nature of the adsorption process. The Freundlich isotherm model, which accounts for multilayer adsorption on heterogeneous surfaces, also demonstrated a reasonably good fit with R^2 = 0.836. Although the Freundlich constant (K_F = 85.159 (mg/g).(L.mg)$^{1/n}$) indicates high adsorption intensity, the heterogeneity index (n^{-1} = 1.417) exceeds unity, suggesting that the adsorption is less favorable to represent by this model [22,25].

Table 1. PRW characteristic obtained from Refinery Unit VI, PT. Pertamina Balongan, West Java, Indonesia.

Parameter	Unit	Value
Turbidity	NTU	10.4
TSS	mg/L	77.5
Oil and grease	mg/L	< 2.5
MBAS	mg/L	0.055
BOD	mg/L	30.4
COD	mg/L	72.3
Ammonia	mg/L	24
Hardness as $CaCO_3$	mg/L	2680
Salinity	mg/L	23.9
Calcium (Ca)	mg/L	636
Magnesium (Mg)	mg/L	159
TOC	-	22.2

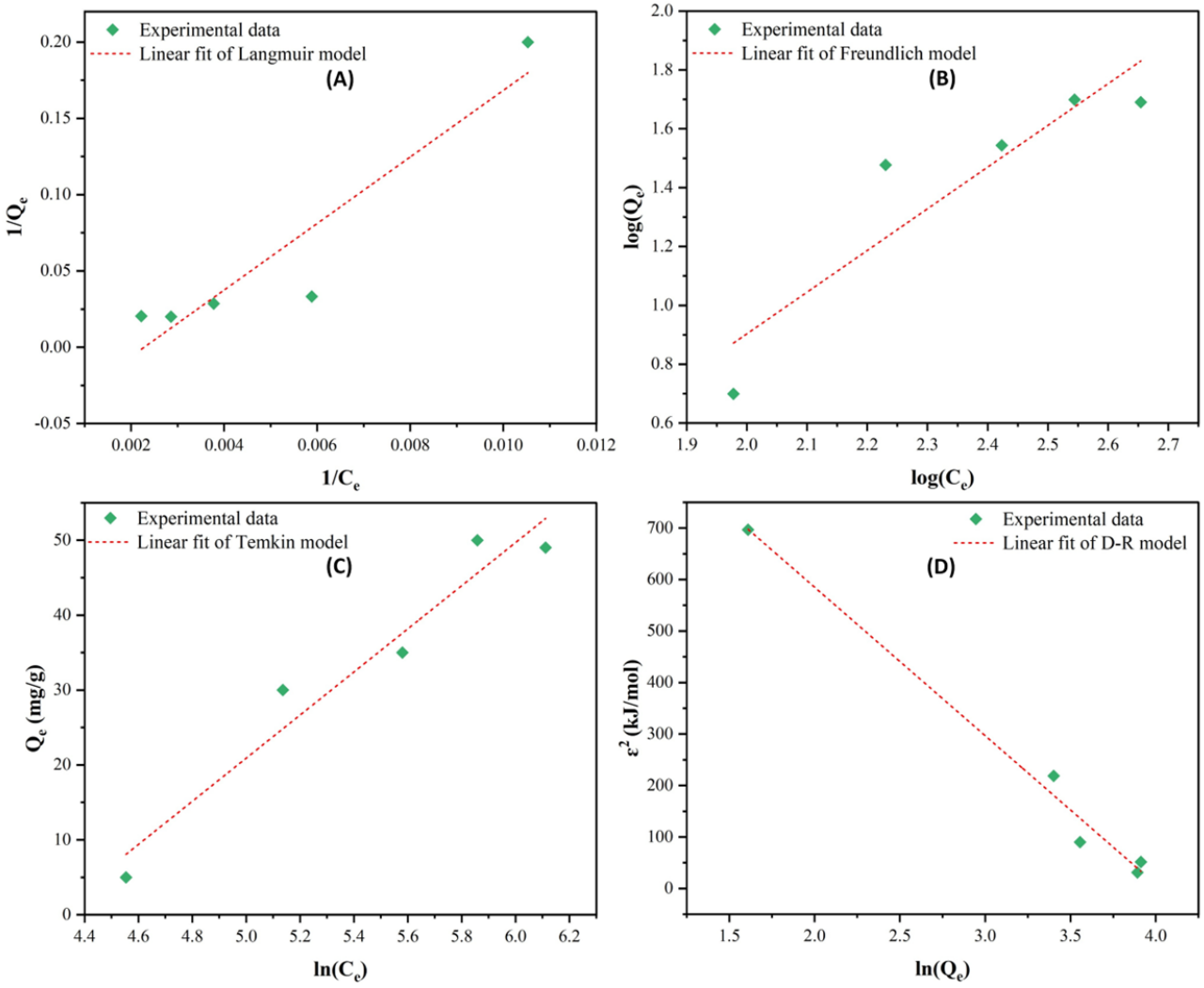

Figure 5. (A) Langmuir, (B) Freundlich, (C) Temkin, (D) Dubinin-RadushKevich isotherm adsorption models of W-based POM composite.

Interestingly, the Temkin isotherm model exhibited a high enough correlation coefficient (R^2 = 0.942), implying a superior fit to the equilibrium data. This model accounts for indirect adsorbate–adsorbent interactions and assumes that the heat of adsorption decreases linearly with increasing coverage. The Temkin constants b_T = 87.569 J/mol and K_T = 71.766 L/mg indicate high interaction energy, supporting the assumption of physisorption dominated by electrostatic interactions [35]. The Dubinin–Radushkevich (D-R) isotherm model, which is often used to distinguish between physical and chemical adsorption, yielded a maximum sorption capacity (Q_m) of 55.640 mg/g with most high correlation coefficient (R^2 = 0.987). The mean adsorption energy (E) was calculated as 8.575 kJ/mol, which is in the range of ion-exchange mechanism indicator (8-16 kJ/mol) [23]. In line with the Temkin evaluation results, the D-R isotherm model also suggests that the adsorption process is dominated by electrostatic (exchange-driven) interactions, emphasizing the importance of adsorbate–adsorbent charge conditioning throughout the adsorption process. In conclusion, the isotherm analysis reveals that the adsorption of contaminants from produced water onto the W-based POM composite is best described by the D-R and Temkin models, indicating a process governed by an ion-exchange mechanism along with a decrease in adsorption energy as surface coverage increases [21,35]. The results also confirm that physisorption may contribute to the overall mechanism, with both monolayer and heterogeneous surface interactions described by the Langmuir and Freundlich models, respectively. These findings provide valuable insight into the surface interaction characteristics of W-based POM and further validate its potential for application in industrial wastewater treatment.

Table 2. (Adsorption isotherm modeling of produced water removal using W-based POM composite.

Isotherm models	Parameters	W-based POM
Langmuir	Q_m (mg/g)	20.125
	K_L (L/mg)	0.002
	R_L	0.479-0.821
	R^2	0.8775
Freundlich	K_F (mg/g).(L.mg)$^{1/n}$	85.159
	n^{-1}	1.417
	R^2	0.836
Temkin	b_T (J/mol)	87.569
	K_T (L/mg)	71.766
	R^2	0.942
Dubinin-Radushkevich (D-R)	Q_m (mg/g)	55.640
	β (mol^2/kJ^2)	0.003
	E (kJ/mol)	8.575
	R^2	0.987

3.2.3. Adsorption kinetic evaluation of produced water degradation using the W-based POM composite

To elucidate the underlying degradation mechanism of produced water by the W-based POM composite, a comprehensive adsorption kinetic study on NH_3-N was conducted using various established models, including pseudo-first-order, pseudo-second-order, intraparticle diffusion, Elovich, and Bangham's models are summarized in Table 3 and Figure 6 (A-E) [22]. This kinetic evaluation was intentionally extended beyond conventional pseudo-first-order assumptions to obtain a more realistic interpretation of the photocatalytic removal behavior in the complex produced water matrix. The kinetic parameters and regression coefficients (R^2) derived from the experimental data are summarized in Table 2. The pseudo-first-order model demonstrated a strong correlation with the experimental data, with a high correlation coefficient (R^2 = 0.986) and an equilibrium adsorption capacity (Q_e) of 46.730 mg/g. This indicates that the degradation process is predominantly governed by physical adsorption involving van der Waals forces or weak electrostatic interactions [21]. In contrast, the pseudo-second-order model yielded a significantly lower R^2 value of 0.446 and an underestimated Q_e of 34.82 mg/g, suggesting that chemisorption plays a less significant role in the degradation pathway for this system [25]. The intraparticle diffusion model yielded the highest R^2 value (0.988), implying that diffusion within the pores of the W-based POM structure constitutes the rate-limiting step of the adsorption process. The calculated intraparticle diffusion constant (K_{id} = 0.260) and intercept (C_i = 0.607) further suggest that although intraparticle diffusion is prominent, surface adsorption may also contribute in the initial stages, as indicated by the non-zero intercept. Evaluation using the Elovich model yielded a moderate R^2 of 0.732, reflecting a less satisfactory fit. This implies that heterogeneous surface adsorption with energetic variability may occur, but it is not the dominant mechanism in this system. However, the relatively low Elovich constant (α = 8.849 mg/g.min and β = 0.249 g/mg) indicate a relatively low activation energy barrier for initial adsorption. Bangham's model exhibited an excellent correlation with the experimental data (R^2 = 0.9870), further reinforcing the importance of pore diffusion and confirming that the adsorption process is not solely limited by surface phenomena but also by the transport of molecules into the porous matrix of W-based POM [26]. In summary, the kinetic study reveals that

the produced water degradation by W-based POM follows a multi-mechanistic pathway, with intraparticle diffusion playing a pivotal role, supplemented by significant contributions from physical adsorption and external mass transfer. These findings provide critical insights into the adsorption dynamics of W-based POM and suggest avenues for further optimizing composite design and process conditions for enhanced photocatalytic wastewater treatment.

3.2.4. Reusability and stability of W-based POM composite

Figure 7 illustrates the variation in the concentration ratio C_t/C_0 over time for each cycle, where C_0 and C_t represent the initial and residual concentrations of the pollutant, respectively. In the first cycle, the photocatalyst demonstrated a significant reduction in C_t/C_0, reaching approximately 0.68 after 120 minutes, indicating

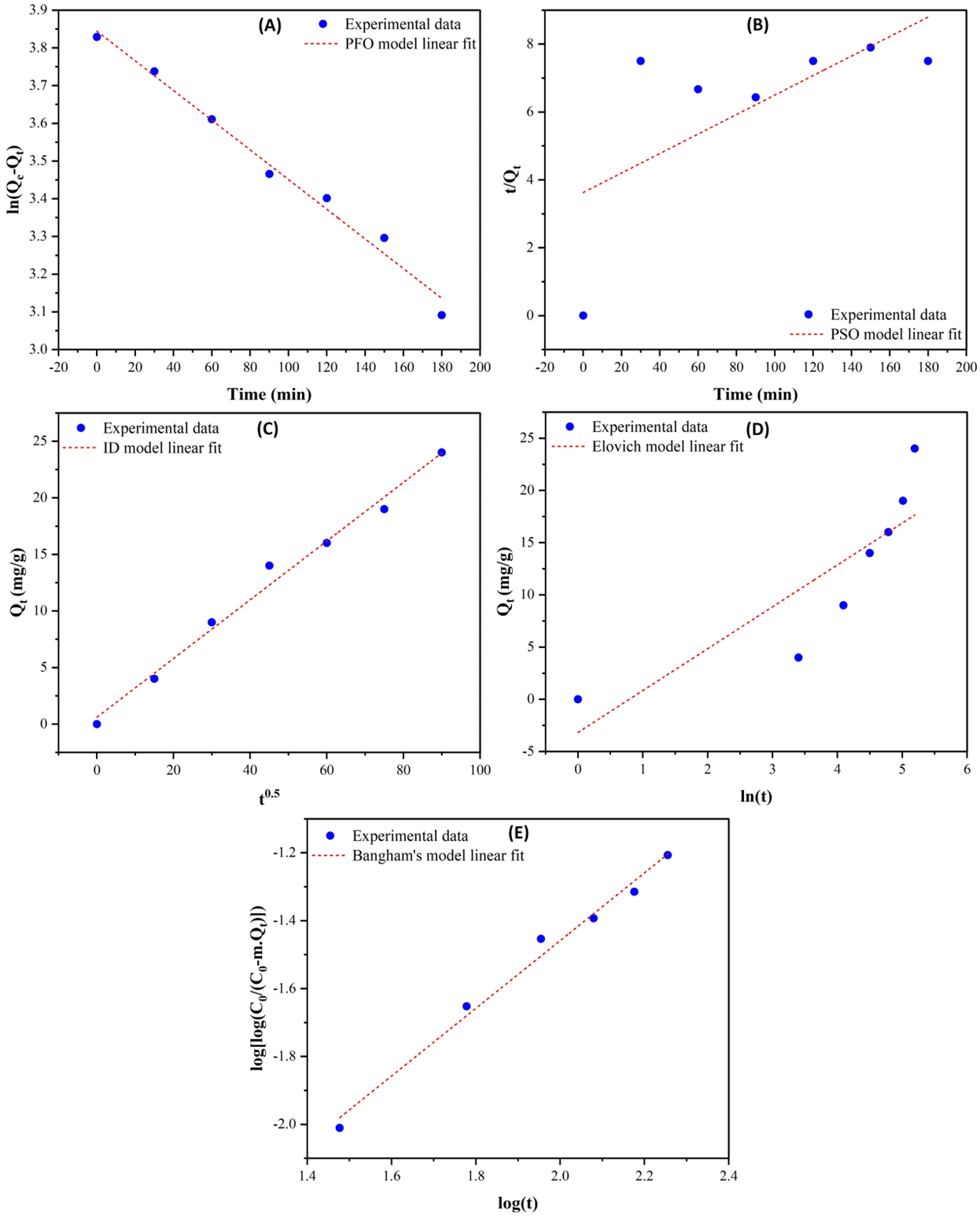

Figure 6. (A) Pseudo-first order, (B) Pseudo-second order, (C) Intraparticle diffusion, (D) Elovich, (E) Bangham's kinetic models of W-based POM composite.

high photocatalytic activity. Upon initiating the second and third cycles, the composite retained a consistent degradation profile, with terminal C_t/C_0 values of approximately 0.59 and 0.61, respectively. These results suggest that the photocatalytic activity of W-based POM was effectively maintained over multiple operational cycles with only a slight decline in performance, likely attributable to surface fouling, minor structural fatigue, or incomplete regeneration between cycles [29]. The minimal reduction in efficiency across cycles may be linked to the partial deactivation of active sites, which is common in POM materials due to adsorbed intermediates or byproducts that block reactive surface regions. However, the observed stability underscores the robustness of the W-based POM framework, particularly its resistance to photocorrosion and its capacity to withstand repetitive light-induced excitation without significant deterioration of its catalytic centers. Moreover, the nearly overlapping degradation trends between cycles affirm the structural integrity and chemical stability of the W-based POM composite. The performance consistency implies minimal leaching of tungsten species and negligible collapse of the POM lattice structure, which is critical for preserving its adsorption and photocatalytic functionalities. These findings are in alignment with prior reports on the stability of tungsten-based POMs, which have demonstrated excellent recyclability and resistance to thermal and chemical stress during extended photocatalytic operations [14,27,29]. From a practical standpoint, the strong reusability of W-based POM suggests its promise for deployment in continuous or semi-continuous flow systems for industrial wastewater treatment, where catalyst longevity is essential for minimizing operational costs and environmental impact. In conclusion, the W-based POM composite exhibits excellent reusability and operational stability over three photocatalytic cycles, making it a viable and sustainable photocatalyst for the treatment of produced water. Its performance consistency positions it as a strong candidate for scalable applications in advanced water purification technologies.

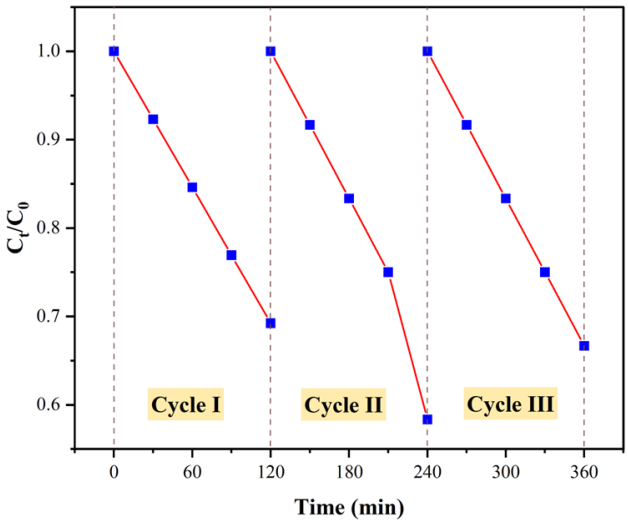

Figure 7. Cycle test evaluation of W-based POM performance.

3.3. Comparison with Previously Reported Photocatalysts

A comparison of the W-based polyoxometalate (POM) photocatalyst developed in this study with previously reported photocatalysts for oilfield produced water (OPW) treatment reveals significant performance enhancements are summarize din Table 4. Previous studies using Bi- or Ti-based photocatalysts, such as $Bi_5O_7Br_{0.5}I_{0.5}$ demonstrated moderate removal efficiencies for phenol (40%), bisphenol A (35%), and COD (65%) under visible-light irradiation [36]. Ag-doped $WO_3/BiVO_4$ achieved higher pollutant removal, with phenol and NH_3-N efficiencies of 81.51% and 84.63%, respectively, under visible light after 5 hours [37]. However, these systems still require relatively long operational times or high catalyst loadings to achieve satisfactory results, particularly when dealing with complex OPW matrices. In addition, co-doped systems such as W(0.5%)/Mo(1.5%) $BiVO_4$ and TiO_2-WO_3@GO composites showed moderate performance for the degradation of hydrolyzed polyacrylamide (HPAM) and total organic carbon (TOC), with removal efficiencies of 43% and 27.7% within 3–4 hours, respectively [38,39]. These findings indicate that while doping or composite strategies can enhance photocatalytic activity, conventional photocatalysts still face challenges in efficiently treating real OPW containing multiple

Table 3. Adsorption kinetic evaluation of produced water degradation using the W-based POM composite.

Kinetic Models	Parameter	W-based POM
Pseudo-first order	K_1 (min^{-1})	0.004
	Q_e ($mg.g^{-1}$)	46.730
	R^2	0.986
Pseudo-second order	K_2 ($g.mg^{-1}.min^{-1}$)	0.0002
	Q_e ($mg.g^{-1}$)	34.819
	R^2	0.446
Intraparticle diffusion	K_{id} ($(mg.(g.min)^{0.5}$)	0.260
	C_i	0.607
	R^2	0.988
Elovich	α ($mg.g^{-1}.min^{-1}$)	8.849
	β ($g.mg^{-1}$)	0.249
	R^2	0.732
Bangham's	k	0.0004
	R^2	0.987

contaminants with different chemical properties. Limitations in charge separation, active site accessibility, and light absorption range contribute to suboptimal performance in these earlier materials.

The W-based POM developed in this study addresses these limitations by achieving remarkable removal efficiencies of 90% for NH_3-N and 84% for TDS within 180 minutes under UV light. This superior performance can be attributed to the optimized electronic structure and redox properties of the POM framework, which enhance charge carrier separation and facilitate the generation of reactive oxidative species. The material's band gap of 2.25 eV allows efficient UV light absorption, providing sufficient oxidative potential for degrading complex pollutants typically found in OPW. Compared to previous Bi- and Ti-based systems, the W-based POM requires a lower catalyst dosage (0.3 g) and shorter operational time, reflecting improved surface reactivity and higher pollutant–catalyst interaction efficiency. Furthermore, the W-based POM demonstrates greater practical applicability for industrial-scale OPW treatment due to its combination of high pollutant removal efficiency, moderate band gap, and reduced operational requirements. These features make the material more amenable to scaling up, offering a promising pathway for process intensification strategies in wastewater treatment. The ability to efficiently remove both NH_3-N and TDS highlights the material's versatility and positions it as a competitive alternative to traditional photocatalysts. Future work can focus on expanding the photocatalytic response to visible light and enhancing catalyst recyclability, further increasing the techno-economic feasibility and sustainability of the system.

4. Conclusion

A novel W-based polyoxometalate (POM) composite was successfully synthesized via a solvothermal method using sodium tungstate dihydrate ($Na_2WO_4 \cdot 2H_2O$) and N,N-dimethylformamide (DMF) as precursors. Morphological characterization revealed a rhombic polyhedral structure with tapered ends and a broad midsection, while elemental mapping showed spatial separation of tungsten (W), confirming the formation of tungstate salts and a well-defined 3D POM framework. XRD analysis uncovered a unique structural characteristic, compressive lattice strain, which is indicative of enhanced charge transport and suppressed electron–hole recombination. In addition, the significantly reduced crystallite size (14.8 nm) suggested an increased surface area, beneficial for photocatalytic degradation. Optical characterization demonstrated a red-shift in the absorption edge, with the band gap energy decreasing from 2.80 eV (bulk WO_3) to 2.25 eV in the composite, reflecting improved visible-light absorption. These structural and optical enhancements endowed the composite with superior photocatalytic performance in treating produced water contaminated with various pollutants. An optimal catalyst dosage of 0.3 g was found effective for treating produced water, achieving removal efficiencies of 90% (NH_3-N) and 84% (TDS), after 180 minutes of UV-light irradiation. Adsorption studies revealed that the

Table 4. Comparison with previous studies.

Photocatalyst	Feed water	Pollutant	Band Gap	Features	Ref.
$Bi_5O_7Br_{0.5}I_{0.5}$	Real OPW	Phenol, BPA, and COD	2.03 eV	Visible-light irradiation removal of phenol = 40%, BPA = 35%, COD = 65%	[36]
Ag-doped $WO_3/BiVO_4$	Oilfield produced water	Phenol and NH_3-N	2.23 eV	Under visible light after 5 h: Phenol removal = 81.51 % and NH_3-N removal = 84.63 %	[37]
W(0.5 %)/Mo(1.5 %) co-doped $BiVO_4$	Oilfield wastewater	Hydrolyzed polyacrylamide (HPAM)	Not reported	Under UV–Visible light after 3 h: Removal = 43 %	[38]
TiO_2-WO_3@GO	Oilfield produced water	Total Organic Carbon (TOC), Organic dyes	~2.6–2.7 eV	27.7 % TOC degradation in 4 h using TiO_2-WO_3@GO composite	[39]
W-based POM	Oilfield produced water	NH_3-N and TDS	2.25 eV	A composite dose of 0.3 g removed 90% NH_3-N and 84% TDS from produced water in 180 min under UV light.	[This study]

Dubinin–Radushkevich and Temkin isotherm models provided the best fit, indicating an ion-exchange-driven interaction mechanism between adsorbate and adsorbent. Furthermore, kinetic analysis suggested a multi-step mechanism, with intraparticle diffusion playing a dominant role. Finally, the stability and reusability assessment confirmed that the composite retained its structural integrity and activity over three consecutive cycles, highlighting its potential as a robust and scalable material for advanced water purification technologies.

Acknowledgment

This project is financially supported by the grant of research of world Class University (RWCU UNDIP) No. 222-764/UN7.D2/PP/IV/2025. Special gratitude to the Institute for Research and Community Services, Diponegoro University (LPPM UNDIP) for the assistance during the completion of this project.

CRedit Author Statement

Author Contributions: T.D. Kusworo: Conceptualization, Methodology, Investigation, Resources, Data Curation, Writing, Review and Editing, Supervision; A.C. Kumoro: Conceptualization, Methodology, Formal Analysis, Data Curation, Writting Draft Preparation, Visualization, Software, Project Administration; A. Veda: Investigation, Writing, Review and Editing, Data Curation; R. Mafazan: Investigation, Writing, Review and Editing, Data Curation; D.A. Azizah: Writing, Review and Editing, Validation. M.B. Puspa: Writing, Review and Editing, Validation. All authors have read and agreed to the published version of the manuscript.

References

[1] Mekonnen, M., Hoekstra, A. (2016) Four billion people facing severe water scarcity, *Science Advances*, 2, e1500323–e1500323. DOI: 10.1126/sciadv.1500323.

[2] Melaibari, A.A., Elamoudi, A.S., Mostafa, M.E., Abu-Hamdeh, N.H. (2023) Utilization of various waste sources in Saudi Arabia as a new clean and renewable energy source: Adsorption of phenol pollutants and removal from petroleum industrial wastes via molecular dynamics simulation, *Engineering Analysis with Boundary Elements*, 147, 164–170. DOI: 10.1016/j.enganabound.2022.12.010.

[3] Ratman, I., Kusworo, T.D., Utomo, D.P., Azizah, D.A., Ayodyasena, W.A. Petroleum Refinery Wastewater Treatment using Three Steps Modified Nanohybrid Membrane Coupled with Ozonation as Integrated Pre-treatment, *Journal of Environmental Chemical Engineering*, 8 (4). DOI: 10.1016/j.jece.2020.103978.

[4] Parkson Corporation, (2025) Wastewater Treatment in Oil Refineries (n.d.)., Water Online. Accessed: Jan. 08, 2025. [Online]. Available: https://www.wateronline.com/doc/wastewater-treatment-in-oil-refineries-0001

[5] Jala, A., Dutta, R., Josyula, J.V.N., Mutheneni, S.R., Borkar, R.M. (2023) Environmental phenol exposure associates with urine metabolome alteration in young Northeast Indian females, *Chemosphere*, 317, 137830. DOI: 10.1016/j.chemosphere.2023.137830.

[6] Huang, X., Li, Z., Zhang, T., Zhu, J., Wang, X., Nie, M., Harada, K., Zhang, J., Zou, X. (2023) Research progress in human biological monitoring of aromatic hydrocarbon with emphasis on the analytical technology of biomarkers, *Ecotoxicology and Environmental Safety*, 257, 114917. DOI: 10.1016/j.ecoenv.2023.114917.

[7] Joshi, N.C., Gururani, P. (2024) A mini review on heavy metal contamination in vegetable crops, *International Journal of Environmental Analytical Chemistry*, 104 (20), 8708–8719. DOI: 10.1080/03067319.2023.2210058.

[8] Hariri, M.B., Botte, G.G. (2023) Simultaneous Removal of Ammonia and Nitrate from Wastewater Using a Pulse Electrolysis Technique, *Journal of The Electrochemical Society*, 170 (5), 053502. DOI: 10.1149/1945-7111/accc57.

[9] Hansen, H.K., Peña, S.F., Gutiérrez, C., Lazo, A., Lazo, P., Ottosen, L.M. (2019) Selenium removal from petroleum refinery wastewater using an electrocoagulation technique, *Journal of Hazardous Materials*, 364, 78–81. DOI: 10.1016/j.jhazmat.2018.09.090.

[10] Zhao, C., Zhou, J., Yan, Y., Yang, L., Xing, G., Li, H., Wu, P., Wang, M., Zheng, H. (2021) Application of coagulation/flocculation in oily wastewater treatment: A review, *Science of The Total Environment*, 765, 142795. DOI: 10.1016/j.scitotenv.2020.142795.

[11] Domingos, R. de A., da Fonseca, F.V. (2018) Evaluation of adsorbent and ion exchange resins for removal of organic matter from petroleum refinery wastewaters aiming to increase water reuse, *Journal of Environmental Management*, 214, 362–369. DOI: 10.1016/j.jenvman.2018.03.022.

[12] Chen, C., Yan, X., Xu, Y., Yoza, B.A., Wang, X., Kou, Y., Ye, H., Wang, Q., Li, Q.X. (2019) Activated petroleum waste sludge biochar for efficient catalytic ozonation of refinery wastewater, *Science of The Total Environment*, 651, 2631–2640. DOI: 10.1016/j.scitotenv.2018.10.131.

[13] Costa, S.I.G., Ferreira, F.L., Weschenfelder, S.E., Fuck, J.V.R., de F.R. da Cunha, M., Marinho, B.A., Mazur, L.P., da Silva, A., de Souza, S.M.A.G.U., de Souza, A.A.U. (2023) Towards the removal of soluble organic compounds present in oilfield produced water by advanced oxidation processes: Critical review and future directions, *Process Safety and Environmental Protection*, 174, 608–626. DOI: 10.1016/j.psep.2023.04.032.

[14] Samuel, O., Othman, M.H.D., Kamaludin, R., Sinsamphanh, O., Abdullah, H., Puteh, M.H., Kurniawan, T.A. (2022) WO3–based photocatalysts: A review on synthesis, performance enhancement and photocatalytic memory for environmental applications, *Ceramics International*, 48 (5), 5845–5875. DOI: 10.1016/j.ceramint.2021.11.158.

[15] Piriyanon, J., Takhai, P., Patta, S., Chankhanittha, T., Senasu, T., Nijpanich, S., Juabrum, S., Chanlek, N., Nanan. S. (2021) Performance of sunlight responsive WO3/AgBr heterojunction photocatalyst toward degradation of Rhodamine B dye and ofloxacin antibiotic, *Optical Materials*, 121, 111573. DOI: 10.1016/j.optmat.2021.111573.

[16] Li, H., Xue, S., Cao, Y., Yue, X., Zhang, A., Chen, C. (2023) Visible light-induced catalytic performance of composite photocatalyst synthesized with nanomaterials WO3 and two-dimensional ultrathin g-C3N4, *Water Science & Technology*, 88(7), 1910–1925. DOI: 10.2166/wst.2023.313.

[17] Li, H., Xue, S., Cao, Y., Yue, X., Zhang, A., Chen, C. (2020) Photocatalytic reduction of Cr(VI) by WO(3)@PVP with elevated conduction band level and improved charge carrier separation property., *Environ. Sci. Ecotechnol.*, 3, 100034. DOI: 10.1016/j.ese.2020.100034.

[18] Chen, J., Ma, Y., Zhang, D., Yang, Y., Bera, M.K., Luo, J., Raee, E., Liu, T. (2020) Ion-pairs of structurally related polyoxotantalate clusters and divalent metal cations, *Journal of Coordination Chemistry*, 73(17–19), 2579–2589. DOI: 10.1080/00958972.2020.1830073.

[19] Orooji, Y., Tanhaei, B., Ayati, A., Tabrizi, S.H., Alizadeh, M., Bamoharram, F.F., Karimi, F., Salmanpour, S., Rouhi, J., Afshar, S., Sillanpää, M., Darabi, R., Karimi-Maleh, H. (2021) Heterogeneous UV-Switchable Au nanoparticles decorated tungstophosphoric acid/TiO2 for efficient photocatalytic degradation process, *Chemosphere*, 281, 130795. DOI: 10.1016/j.chemosphere.2021.130795.

[20] Chen, X., Liu, X., Zhu, L., Tao, X., Wang, X. (2022) One-step fabrication of novel MIL-53(Fe, Al) for synergistic adsorption-photocatalytic degradation of tetracycline, *Chemosphere*, 291, 133032. DOI: 10.1016/j.chemosphere.2021.133032.

[21] Dalanta, F., Kusworo, T.D. (2022) Synergistic adsorption and photocatalytic properties of AC/TiO2/CeO2 composite for phenol and ammonia–nitrogen compound degradations from petroleum refinery wastewater, *Chemical Engineering Journal*, 434, 134687. DOI: 10.1016/j.cej.2022.134687.

[22] Abbas, M. (2021) Factors influencing the adsorption and photocatalysis of direct red 80 in the presence of a TiO_2 : Equilibrium and kinetics modeling, *Journal of Chemical Research*, 45 (7–8), 694–701. DOI: 10.1177/1747519821989969.

[23] Chu, K.H., Hashim, M.A., Hayder, G., Bollinger, J.-C. (2024) Comparative Evaluation of the Dubinin–Radushkevich Isotherm and Its Variants, *Ind. Eng. Chem. Res.*, 63(34), 15002–15011. DOI: 10.1021/acs.iecr.4c01895.

[24] Rosly, N.Z., Ishak, S., Abdullah, A.H., Kamarudin, M.A., Ashari, S.E., Alang Ahmad, S.A. (2022) Fabrication and optimization calix[8]arene-PbS nanoadsorbents for the adsorption of methylene blue: Isotherms, kinetics and thermodynamics studies, *Journal of Saudi Chemical Society*, 26(1), 101402. DOI: 10.1016/j.jscs.2021.101402.

[25] Moawed, E.A., El-Shahat, M.F. (2016) Equilibrium, kinetic and thermodynamic studies of the removal of triphenyl methane dyes from wastewater using iodopolyurethane powder, *Journal of Taibah University for Science*, 10(1), 46–55. DOI: 10.1016/j.jtusci.2015.03.008.

[26] Bakar, S.A., Geedi, H.S., Khamidun, M.H., Mohamed, R.M.S.R., Daud, M.F.C., Md Ali, U.F. (2023) Evaluation lead removal kinetics modelling of adsorption by using composite of Chitosan and Ceramic waste, *IOP Conference Series: Earth and Environmental Science*, 1205 (1), 012010. DOI: 10.1088/1755-1315/1205/1/012010.

[27] Sun, Z., Wang, R., Kozhevnikov, I.V. (2025) Versatile POMOF-based materials: Synthesis, mechanism, topology and catalytic applications, *Coordination Chemistry Reviews*, 524, 216304. DOI: 10.1016/j.ccr.2024.216304.

[28] Maru, K., Kalla, S., Jangir, R. (2022) MOF/POM hybrids as catalysts for organic transformations, *Dalton Trans.*, 51(32), 11952–11986. DOI: 10.1039/D2DT01895K.

[29] Murmu, G., Samajdar, S., Ghosh, S., Shakeela, K., Saha, S. (2024) Tungsten-based Lindqvist and Keggin type polyoxometalates as efficient photocatalysts for degradation of toxic chemical dyes, *Chemosphere*, 346, 140576. DOI: 10.1016/j.chemosphere.2023.140576.

[30] Jahan Tamanna, N., Sahadat Hossain, Md., Mohammed Bahadur, N., Ahmed, S. (2024) Green synthesis of Ag2O & facile synthesis of ZnO and characterization using FTIR, bandgap energy & XRD (Scherrer equation, Williamson-Hall, size-train plot, Monshi- Scherrer model), *Results in Chemistry*, 7, 101313. DOI: 10.1016/j.rechem.2024.101313.

[31] Miao, Y., Zhao, Y., Zhang, S., Shi, R., Zhang, T. (2022) Strain Engineering: A Boosting Strategy for Photocatalysis, *Advanced Materials*, 34 (29), 2200868. DOI: 10.1002/adma.202200868.

[32] Loyola Poul Raj, I., Jegatha Christy, A., David Prabu, R., Chidhambaram, N., Mohd. Shkir, AlFaify, S., Khan, A. (2020) Significance of Ni doping on structure-morphology-photoluminescence, optical and photocatalytic activity of CBD grown ZnO nanowires for opto-photocatalyst applications, *Inorganic Chemistry Communications*, 119, 108082. DOI: 10.1016/j.inoche.2020.108082.

[33] Khan, M.A.M., Khan, W., Ahamed, M., Alhazaa, A.N. (2017) Microstructural properties and enhanced photocatalytic performance of Zn doped CeO2 nanocrystals, *Scientific Reports*, 7 (1), 12560. DOI: 10.1038/s41598-017-11074-7.

[34] Uma, H.B., Ananda, S., Nandaprakash, M.B. (2019) High efficient photocatalytic treatment of textile dye and antibacterial activity via electrochemically synthesized Ni-doped ZnO nano photocatalysts, *Chemical Data Collections*, 24. DOI: 10.1016/j.cdc.2019.100301.

[35] Arabian, S., Gordanshekan, A., Farhadian, M., Nazar, A.R.S., Tangestaninejad, S., Sabzyan, H. (2024) Adsorption/photocatalytic degradation of Cefixime by the green Bi2WO6/g-C3N4/ZIF-67 dual S-scheme heterojunction: Artificial neural network, genetic algorithm, density functional theory, and toxicity assessments, *Chemical Engineering Journal*, 488, 150686. DOI: 10.1016/j.cej.2024.150686.

[36] Bai, Y., Shi, X., Wang, P., Wang, L., Xie, H., Li, Z., Qu, L., Ye, L. (2018) Synthesis of one-dimensional Bi5O7Br0.5I0.5 solid solution for effective real oilfield wastewater treatment via exciton photocatalytic process, *Journal of the Taiwan Institute of Chemical Engineers*, 91, 358–368. DOI: 10.1016/j.jtice.2018.05.045.

[37] Kusworo, T.D., Seng, K.S., Arutanti, O., Puspa, M.B., Hasbullah, H., Dalanta, F. (2026). Visible-light-driven Z-scheme Ag-doped WO3/BiVO4 ternary nanocomposite with a synergistic adsorption-photocatalytic feature for enhanced oil field produced water treatment, *Journal of Water Process Engineering*, 81, 109250. DOI: 10.1016/j.jwpe.2025.109250.

[38] Zhou, Y., Li, W., Wan, W., Zhang, R., Lin, Y. (2015). W/Mo co-doped BiVO4 for photocatalytic treatment of polymer-containing wastewater in oilfield, *Superlattices and Microstructures*, 82, 67–74. DOI: 10.1016/j.spmi.2015.02.011.

[39] Samuel, O., Khan, A.U., Othman, M.H.D., Kurniawan, T.A., Kamaludin, R., Matsuura, T., Imtiaz, A., Rushdan, A.I. (2024) Visible light-driven TiO2-WO3@GO photocatalyst with catalytic memory for round-the-clock photocatalytic degradation of oilfield-produced water, *Ceramics International*, 50 (11), 18205–18219. DOI: 10.1016/j.ceramint.2024.02.305.